Fermilab Library
0 1160 0015252 4
IKP-MS-92-0102

IKP-MS-92/0102

Particle identification in modular electromagnetic calorimeters

F. Berger, D. Bock, G. Clewing, L. Dragon,
R. Glasow, G. Hölker, K. H. Kampert,
T. Peitzmann, M. Purschke, B. Roters, R. Santo,
K. Steffens, D. Stüken and A. Twyhues

ROUTE TO

NAME	LOCATION
~~RAMBERG~~	~~122~~
~~ALBROW~~	~~318~~

RETURN TO FERMI LIBRARY

APR 29 1992

INSTITUT FÜR KERNPHYSIK
UNIVERSITÄT MÜNSTER

preprint IKP-MS-92/0102

Particle identification in modular electromagnetic calorimeters

F. Berger, D. Bock, G. Clewing, L. Dragon,
R. Glasow, G. Hölker, K. H. Kampert,
T. Peitzmann, M. Purschke, B. Roters, R. Santo,
K. Steffens, D. Stüken and A. Twyhues

Abstract

A method to discriminate between electromagnetic and hadronic showers in modular electromagnetic calorimeters is presented. The algorithm is based on the analysis of the lateral dispersion of the shower distribution. Special emphasis is also given to the problem of identifying and unfolding overlapping showers. The performance of the methods has been checked by analyzing experimental data taken with a 7×7 lead glass array at an electron and a pion beam in the energy range from 3 to 40 GeV as well as by analyzing the properties of the reconstructed π^0 peak observed in the two photon invariant mass spectra from heavy-ion reactions.

submitted to Nucl. Instr. Meth.

1 Introduction

The detection of photons or electrons by modular electromagnetic calorimeters has become a standard technique in high-energy physics experiments. A shower induced by photons or electrons is called electromagnetic, and its development in this kind of calorimeter differs considerably from a hadronic shower induced by e.g. pions or protons [1].

In this paper we investigate the capability of particle identification in a finely granulated lead glass array, which is a typical representative of homogeneous electromagnetic calorimeters. Our analysis is based on the fact that the lateral development of hadronic showers is different from that of electromagnetic ones, which is reflected in the dispersion of the shower. We will introduce an improvement of this standard measure of the shower width and discuss the following points :

i. identification of single electromagnetic showers and misidentification of single hadronic ones as photons or electrons,

ii. recognition and unfolding of two overlapping electromagnetic showers,

iii. and recognition of overlap between an electromagnetic and a hadronic shower.

The corresponding identification efficiencies achieved with the proposed method have been determined. For a planar detector configuration covering a large solid angle the method has to be applicable also for non-perpendicular incidence.

In particle physics experiments with soft hadronic interactions the first of these points is of primary interest. The problem (ii) arises only from the two photon decay of energetic π^0 resulting in two close by electromagnetic showers, which may merge into one shower. However, for high particle densities, like in heavy-ion reactions or in particle jets, all items (i – iii.) have to be considered.

In this paper we discuss the performance of our analysis to detect photons, electrons, hadrons, and overlapping showers. In section 2 the experimental setup and the tests, in which the data were obtained, are described. In section 3 we introduce the cluster algorithm used to classify our data. A method to separate electromagnetic from hadronic showers is presented in section 4 and 5. The detection and unfolding of overlapping showers are subject of section 6 and 7. We have applied our algorithm to heavy-ion data and discuss the results in section 8. Section 9 gives a summary.

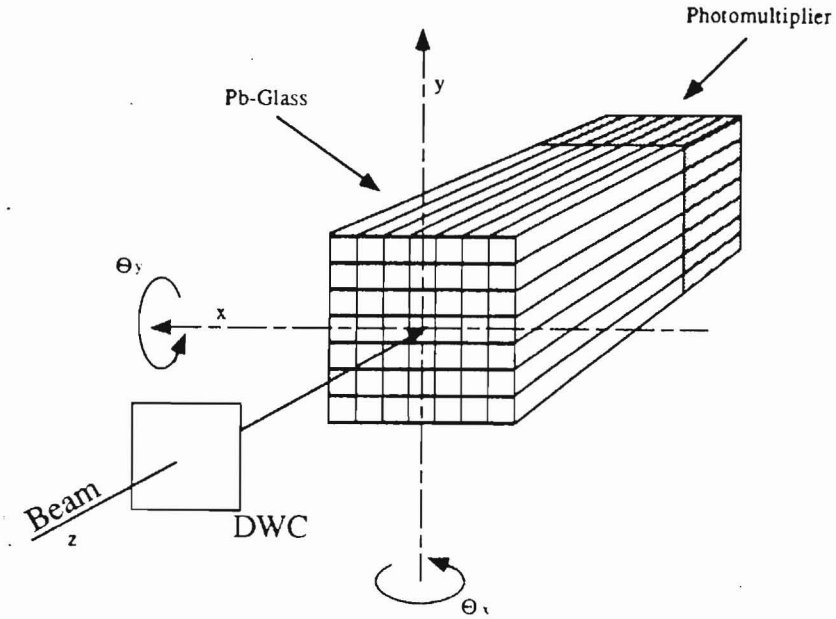

Figure 1: The experimental setup at the SPS X3 beam line. The x and y axis for the rotation is at the front face of the lead glass detector.

2 Apparatus and experimental data

A test was performed with a detector consisting of 7×7 lead glass modules at the SPS X3 beam line in the CERN West Area, using an electron and a negative pion beam in the energy range from 3 to 40 GeV. The detector was placed on a movable platform so that it could be scanned horizontally and vertically through the beam. A rotation around two orthogonal axes was also possible to allow non-perpendicular incidence at the detector front face (see Fig. 1).

Each module is made of TF1 glass with a total length of 40 cm and a cross section of 4×4 cm^2. The radiation length X_0 has been calculated to be 2.78 cm and the interaction length λ to be 38 cm [2], i.e. the length of the modules corresponds to 14.4 X_0 and 1.1 λ. The lead glass blocks were coupled to FEU-84 photomultipliers read out by 11 bit charge sensitive ADCs with automatic pedestal subtraction (LeCroy 2280,System). The energy calibration has been performed by exposing the center of each module to a 10 GeV electron beam. The gains of the photomultipliers have been adjusted to 30 GeV full scale ($\hat{=} -1000$ pC) in a single module and the ADC-values have been corrected for time dependent gain drifts monitored by a laser reference system [3].

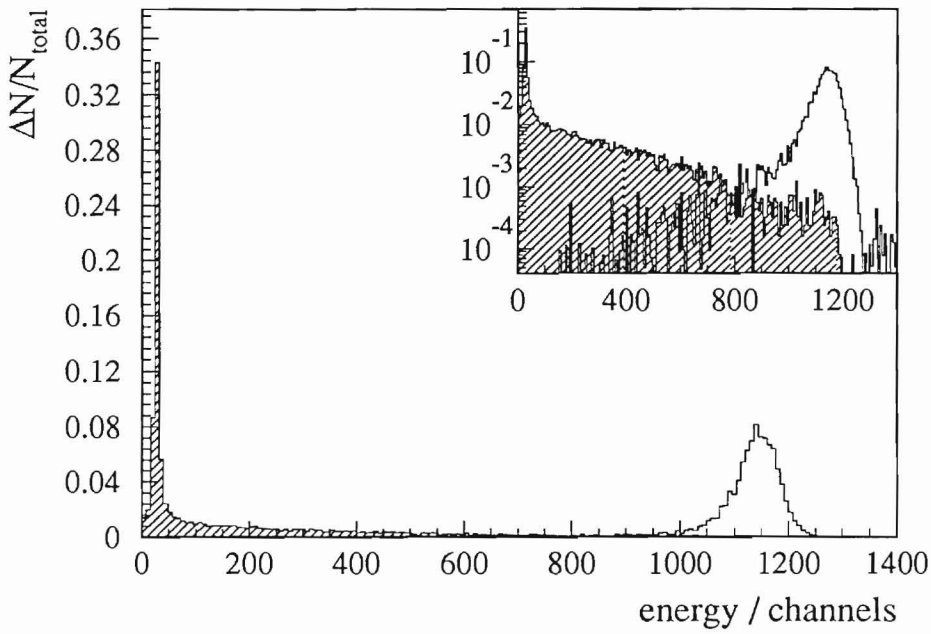

Figure 2: Distribution of the energy response for electrons and charged pions (shaded area) with an incident energy of 20 GeV. The insert shows the same spectrum with a logarithmic y axis.

The SPS X3 beam line is equipped with a magnetic spectrometer, which selects particles of momentum p with an accuracy $\Delta p/p$ of about 1 %. Two gas Čerenkov counters allow to tag electrons and pions. The beam trigger was defined by two scintillators and the beam spot size was 2.5×1.6 cm^2(RMS). The position of the beam particle on the front face of the test detector was measured by a delay-line wire chamber (DWC) with a precision of better than 1 mm in x and y direction. About 9 % of the electrons were found to produce showers in the lead glass, which give either one cluster with two maxima or two clusters with one maximum each (A *cluster* is defined in Sect. 3.). As the ADC-sum of two cluster events gives the same energy deposition and resolution as those electron events giving one cluster with one maximum, these events are interpreted as electrons accompanied by a bremsstrahlung photon [4]. The remaining amount of analyzed data is given in Tab. 1 and 2 for the different incident energies and different angle of incidence combinations.

The efficiency of electron and pion tagging is demonstrated in Fig. 2. Here the total energy deposited by 20 GeV electrons and charged pions (shaded area) is displayed. No electron peak is observed in the pion sample and no minimum ionizing peak in the electron sample.

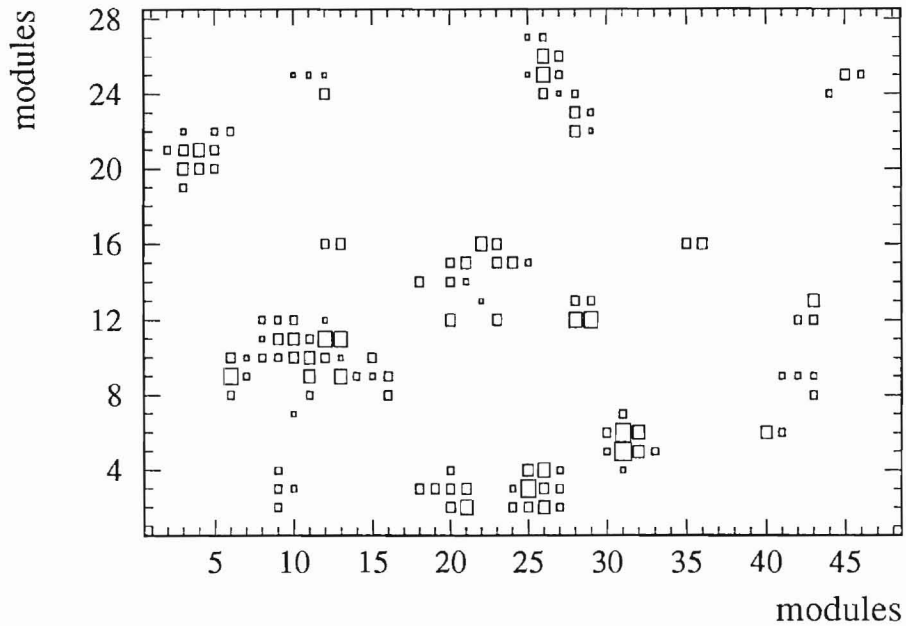

Figure 3: ADC pulse height distributions of the lead glass array SAPHIR for a single 200 A·GeV ^{32}S + Au reaction. Each square corresponds to the logarithmic response of a single lead glass module.

3 Cluster algorithm

A typical single event display showing the two-dimensional pattern of modules with non-zero energy deposition is depicted in Fig. 3. The data were taken with the calorimeter SAPHIR [3] in 200 A·GeV ^{32}S+Au reactions. In order to analyze such events it is mandatory to use a cluster finding routine. The cluster algorithm described in the following is applied to the data taken by the test detector. As the RMS of the pedestal distributions is 1 to 2 channels, only modules with an ADC-value of 2 or more have been considered. Groups of adjacent modules are called clusters. A module with an ADC-value of at least 3 channels higher than all neighboring modules is defined as a cluster maximum. The further analysis is directed according to the number of maxima found within one cluster. Clusters with one maximum are assumed to be single particles whereas those with two or more maxima may indicate an overlap of several showers. Disentangled particles and clusters with one maximum are called *hits*. Fig. 4 shows the flow chart of our particle identification algorithm. The dispersion analysis will be described in the next section, whereas the shower unfolding is explained in Sect. 7.

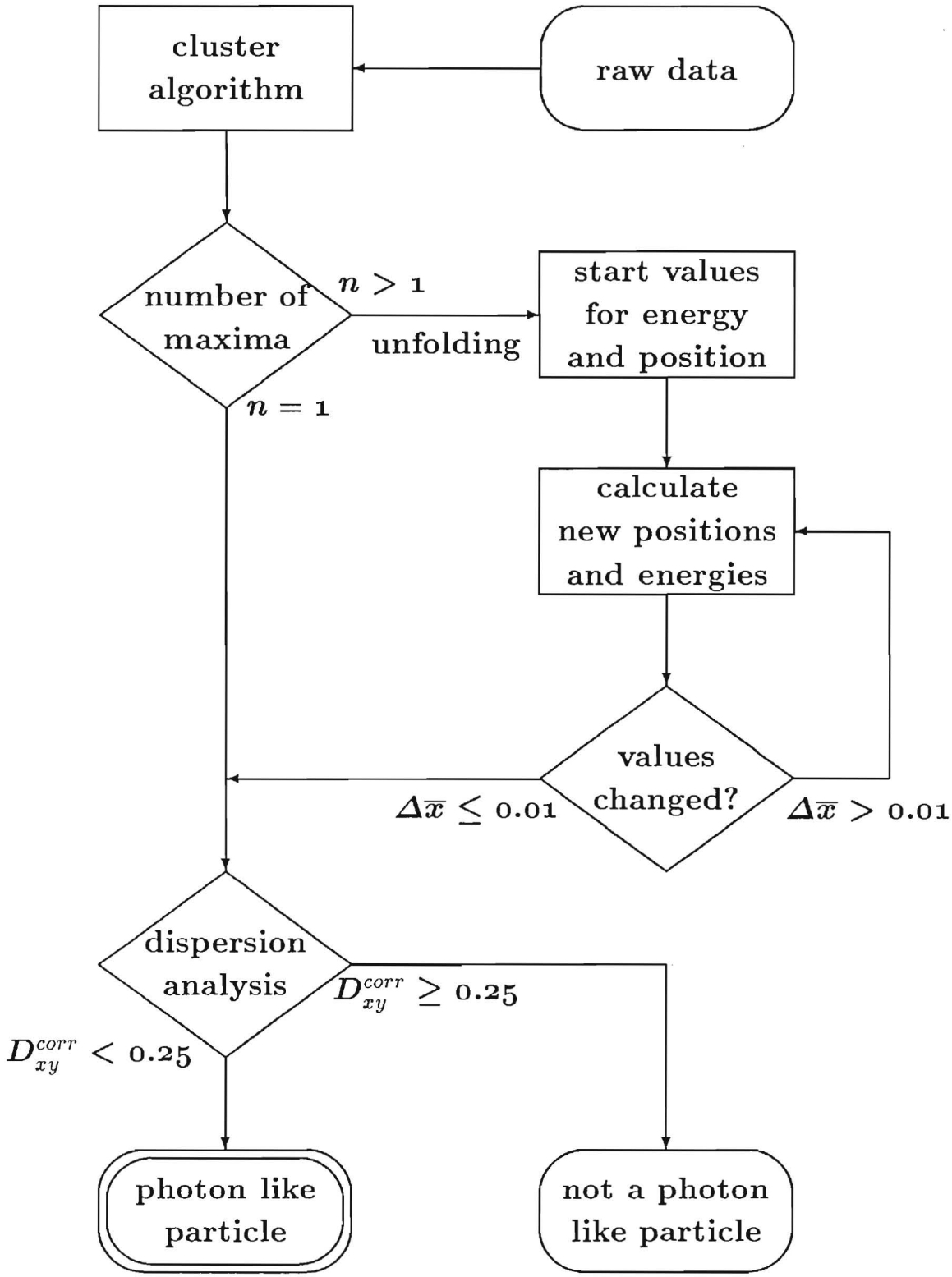

Figure 4: Flow chart of the algorithm used to analyze heavy-ion data. $\Delta\overline{x}$ is the difference of the first moments in module units for two succeeding iterations.

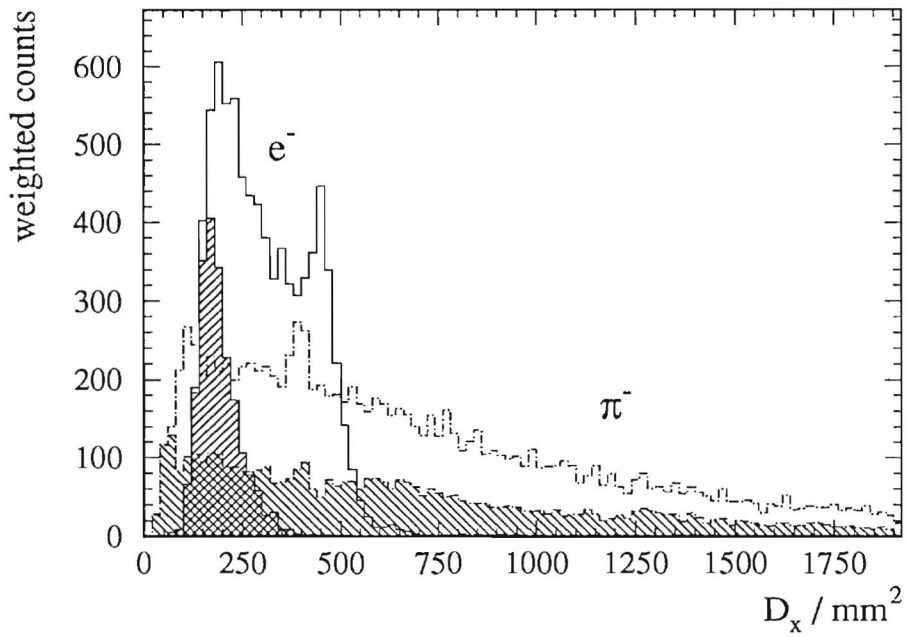

Figure 5: Dispersion D_x distribution for showers produced by electrons (solid line) and negative pions (dashed line) with an incident energy of 20 GeV. The shaded areas correspond to those hits entering the center of the module. No cluster algorithm is applied for this plot.

4 Separation of electrons and negative pions

As mentioned above, electrons and negative pions can be distinguished by the widths of their showers [6]. A frequently used measure of the width is the second central moment of the lateral distribution named dispersion

$$D_x = \frac{\sum A_i x_i^2}{\sum A_i} - \left(\frac{\sum A_i x_i}{\sum A_i}\right)^2 = \overline{x^2} - \overline{x}^2 \tag{1}$$

where A_i is the pulse height in the i-th module and x_i the module position [7]. For simplicity only the projection of the cluster on the x-axis is considered in this section, i.e. in all formulas x can be replaced by y. In Fig. 5 D_x is displayed for electrons (solid line) and pions (dashed line) at an incident energy of 20 GeV. Their points of incidence are uniformly distributed over the detector front face. The narrow electron and the very broad pion distributions offer the possibility to separate electrons and charged pions. Restricting the analysis to particles hitting only the central area of a module results in the shaded histograms in Fig. 5. For this special case the rejection of π^- is more efficient compared to the more realistic case of uniformly distributed hits. The shaded distributions are similar to results given in Ref. [6] where data were taken with the same detector material and

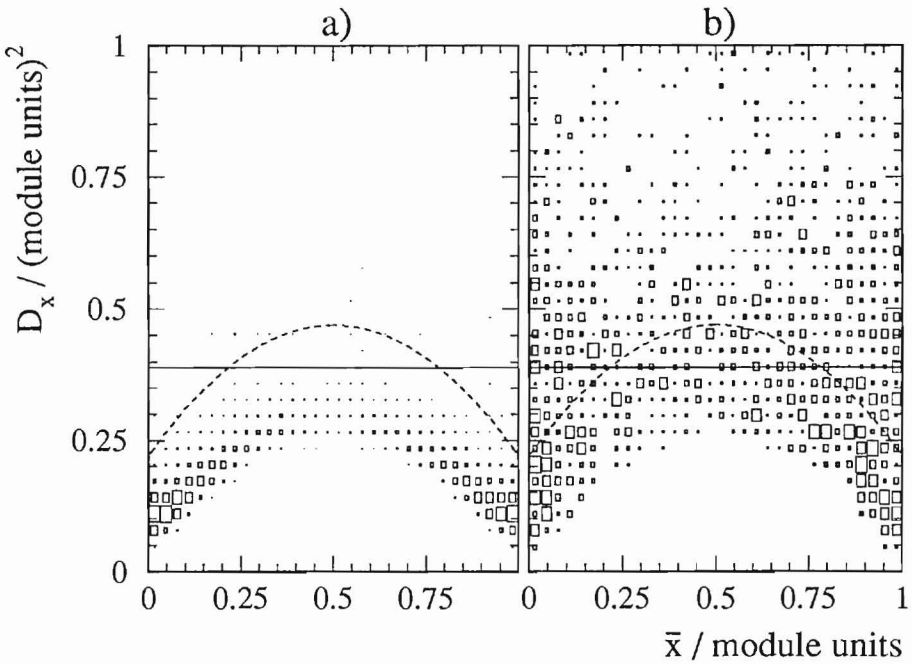

Figure 6: Dispersion D_x for electrons (a) and negative pions (b) as a function of the first moment $\overline{x}$ at 10 GeV deposited energy. The dashed line represents a parabolic cut and the solid line a fixed cut.

a slightly smaller module size. The curves demonstrate also, that the results of Ref. [6] are limited to particles hitting the central area of a detector module. No cluster routine was applied in Fig. 5 in order to be comparable to the results from Ref. [6].

In the following only clusters with one maximum will be analyzed and electron and negative pion clusters will be compared at similar amounts of deposited energy, i.e. the π^- contamination in an electron sample calculated by this selection has to be multiplied by the probability that a charged pion produces a cluster with the considered amount of energy (see Fig. 2). The dependence of D_x for electrons and charged pions on the hit position relative to the module boundaries is shown in Fig. 6. Here D_x is plotted as a function of the first moment $\overline{x}$, which depends on the position relative to the module boundaries [5]. According to the applied coordinate system $\overline{x} = 0$ or 1 means the center and $\overline{x} = 0.5$ the edge of a module. Clusters with only two modules in the x-direction always fulfill the following equation exactly

$$D_x^{min} = -(\overline{x} - x_R)(\overline{x} - x_L), \tag{2}$$

i.e. no particle identification is possible in these cases. Here x_R and x_L are the right and left edges of the central module ($x_L \leq \overline{x} \leq x_R$). If the cluster consists of more than 2 modules in x-direction, $D_x(\overline{x})$ is always larger than $D_x^{min}(\overline{x})$. This threshold leads to the parabolic area without any

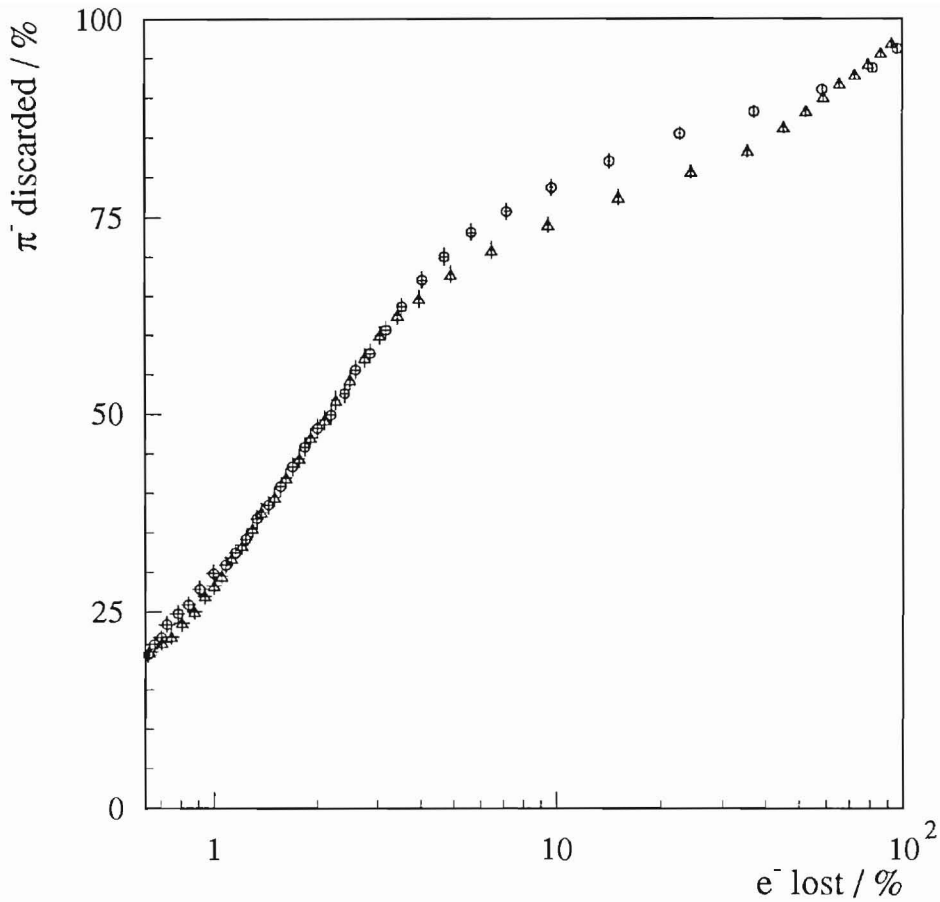

Figure 7: Efficiency to discard pions as a function of the fraction of electron lost by applying a fixed cut (triangle) and a parabolic cut (circles).

entry neither for electrons nor for pions. A very similar behaviour has been observed with a BGO detector [8] underlining that the proposed method is not depending on the detection mechanism of the shower, which is Čerenkov light in the case of lead glass and scintillation light in the case of BGO. In order to reject pions two different cuts for D_x have been compared, a fixed cut (solid line) and a parabolic cut (dashed line, see Fig. 6). Fig. 7 shows the respective efficiencies to discard charged pions as a function of the electron fraction lost by applying the two different cuts. Allowing e.g. 10 % electron loss the hadron suppression can be improved from 73 % to 79 %. Even more critical, the fixed cut leads to a position dependent identification probability for electrons and charged pions, whereas no position dependence is observed for the parabolic cut.

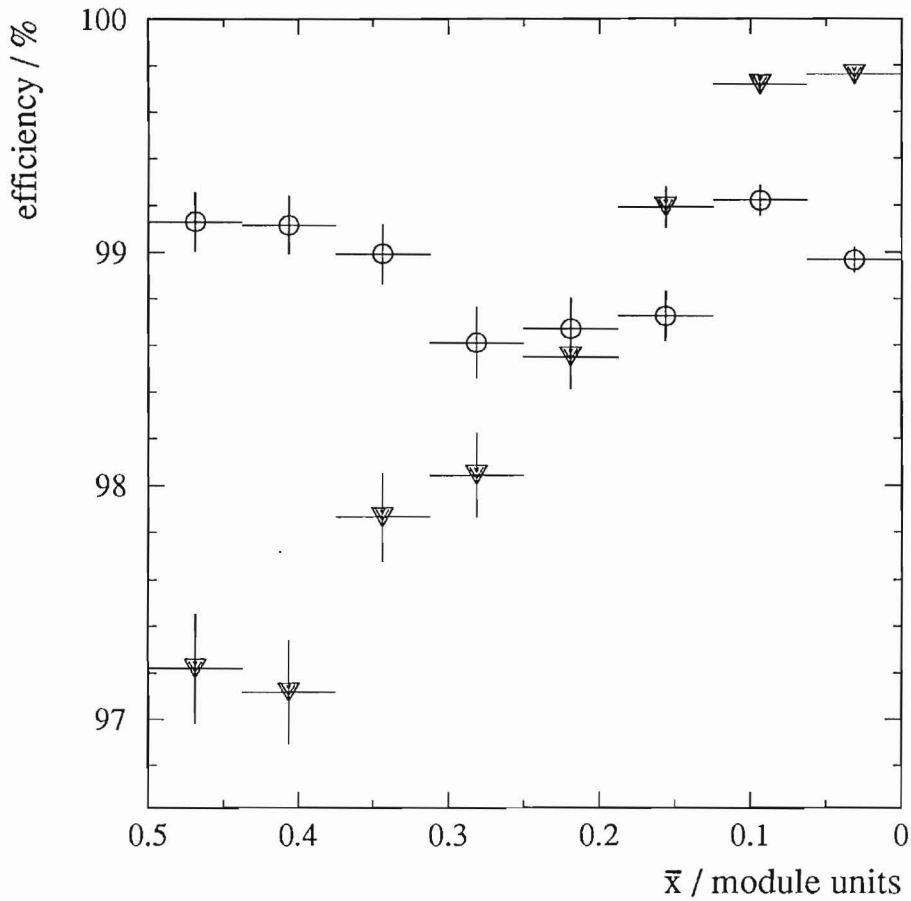

Figure 8: The efficiency to accept electrons as a function of the module position is plotted for the fixed cut (triangles) and the parabolic cut (circles). $\overline{x} = 0$ (0.5) corresponds to the center (edge) of the module. The average efficiency to accept electrons is in both cases 99 %.

This is illustrated in Fig. 8 by plotting the probability to accept an electron as a function of the position within one module for the fixed cut (triangles) and the parabolic cut (circles). Both cuts have the same overall efficiency of 99 % electron acceptance. Therefore we introduce a corrected dispersion D_x^{corr} in the following, which is defined as

$$D_x^{corr} = D_x - D_x^{min}. \tag{3}$$

A cut in the one-dimensional distribution D_x^{corr} is equivalent to a parabolic cut in the two-dimensional distribution of D_x versus $\overline{x}$.

5 Dependence of D_x^{corr} on angle and energy

The dependence of D_x^{corr} on angle and energy has to be analyzed to examine the limitations of this method for various detector configurations. Fig. 9 shows D_x^{corr} distributions for different combinations of (θ_x, θ_y) (see Fig. 1) for electrons with 10 GeV incident energy. The D_x^{corr} distribution does not change very much for angles less than 6°.

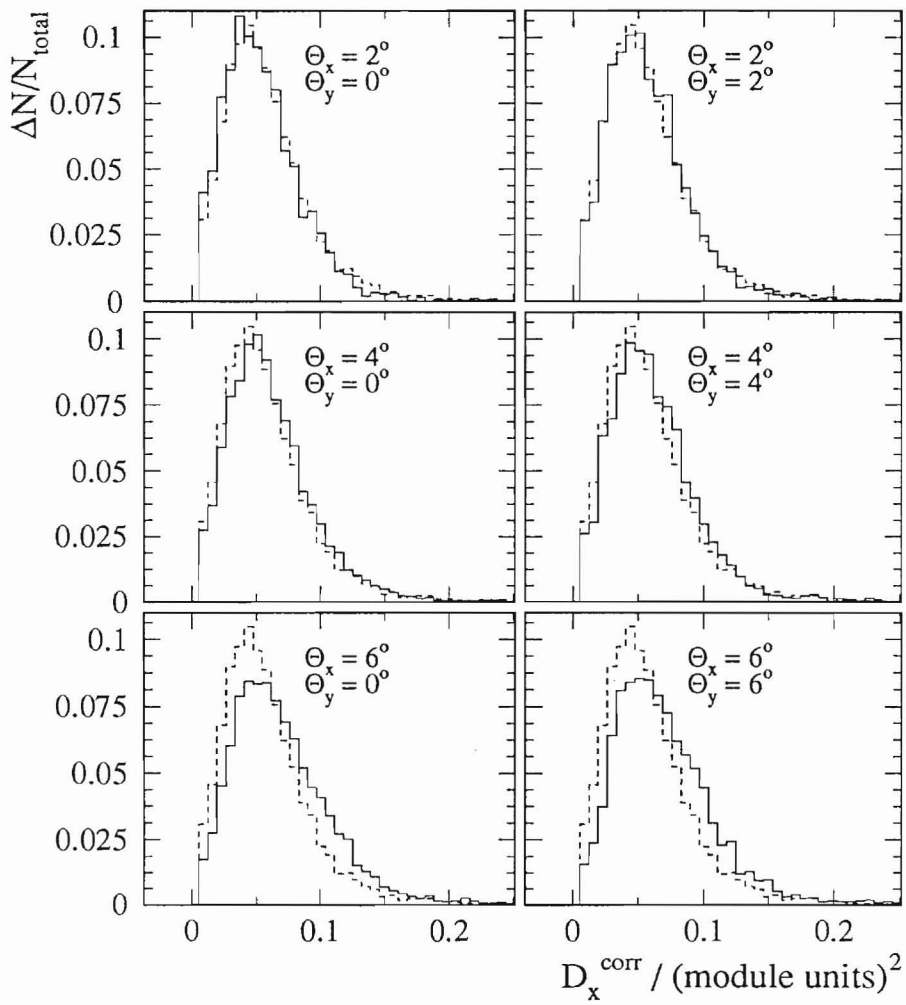

Figure 9: D_x^{corr} distributions for different combinations of angles of incidence (θ_x, θ_y) calculated from 10 GeV electron showers. For comparison the D_x^{corr} distribution for perpendicular incidence is plotted as a dashed histogram.

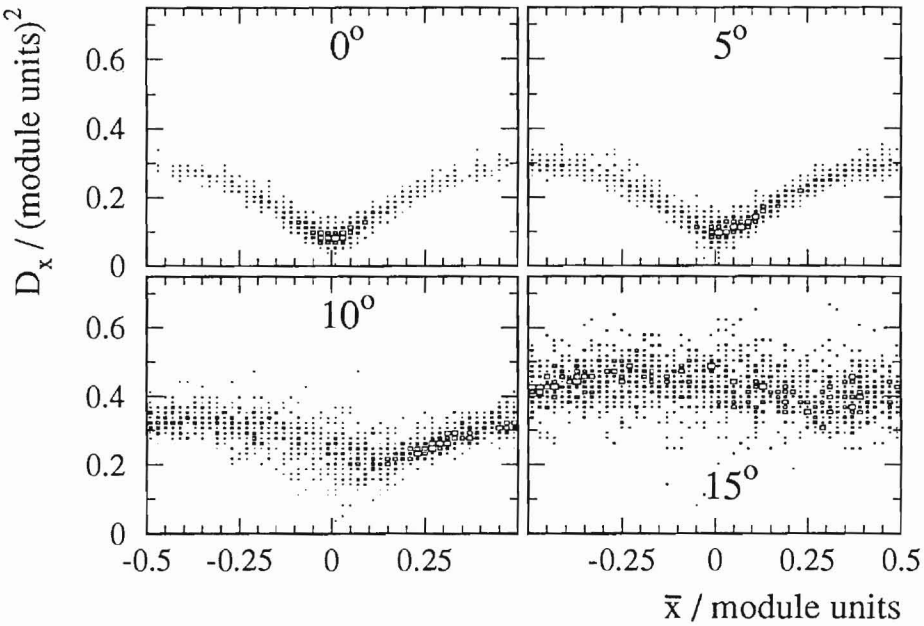

Figure 10: Dispersion D_x as a function of the first moment $\overline{x}$ for different angles of incidence 0°, 5°, 10°, and 15°. The data are simulated using GEANT assuming TF1 lead glass with the same module dimensions as the test detector.

In order to investigate our method for larger angles of incidence electromagnetic showers have been simulated using GEANT [2]. Fig. 10 shows D_x as a function of $\overline{x}$ for four different angles of incidence in the range from 0° to 15°. The results for 0° and 5° reproduce our experimental values of D_x. For larger angles D_x increases and becomes position independent and D_x^{corr} becomes useless. This behaviour reflects that at small angles only two modules contribute significantly to D_x, which is expected as the radial shower profile is mainly exponential [9]. For increasing angles the shower spreads over more modules.

The energy dependence of D_x^{corr} is shown in Fig. 11 for two angle settings and incident energies of 3, 10, 20, and 30 GeV. Serving as a reference the D_x^{corr} distributions of the 10 GeV data are plotted as dashed histograms. D_x^{corr} appears to be slightly energy dependent as the shape of electromagnetic showers depends logarithmically on the energy [10]. The energy-dependence of D_x^{corr} is also influenced by the ADC-cutoff, i.e. more modules above the threshold are involved in high energetic showers than in low energetic ones and hence D_x^{corr} becomes larger with increasing energy. On the other hand, D_x^{corr} of charged pion induced clusters is observed to become smaller for larger amounts of deposited energy (more than 10 GeV). This behaviour of D_x^{corr} implies that the efficiency to discard charged pions as a function of electrons lost is energy dependent.

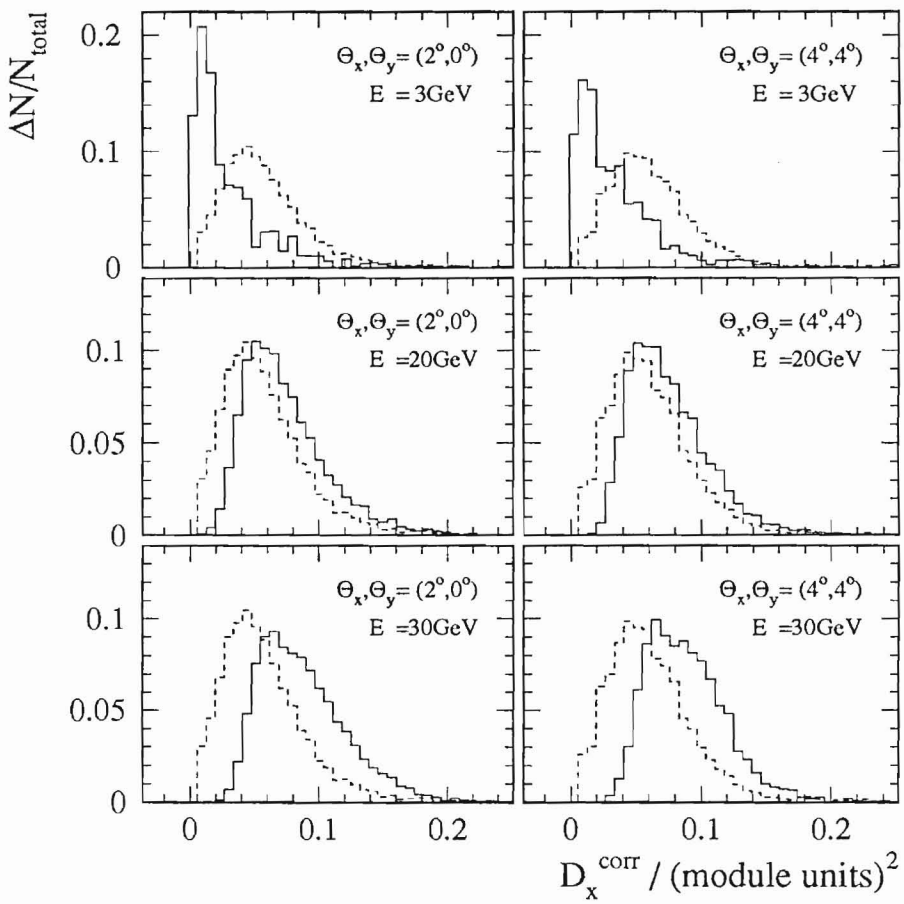

Figure 11: D_x^{corr} distributions for the energies 3 GeV (a), 20 GeV (b), and 30 GeV (c) at two angle of incidence (θ_x, θ_y) settings. For 3 GeV the $(2°, 0°)$ distribution is used because $(0°, 0°)$ data have not been measured. For comparison the result from the 10 GeV dataset is shown as a dashed histogram for the angles $(0°, 0°)$ in the left column and for $(4°, 4°)$ in the right column.

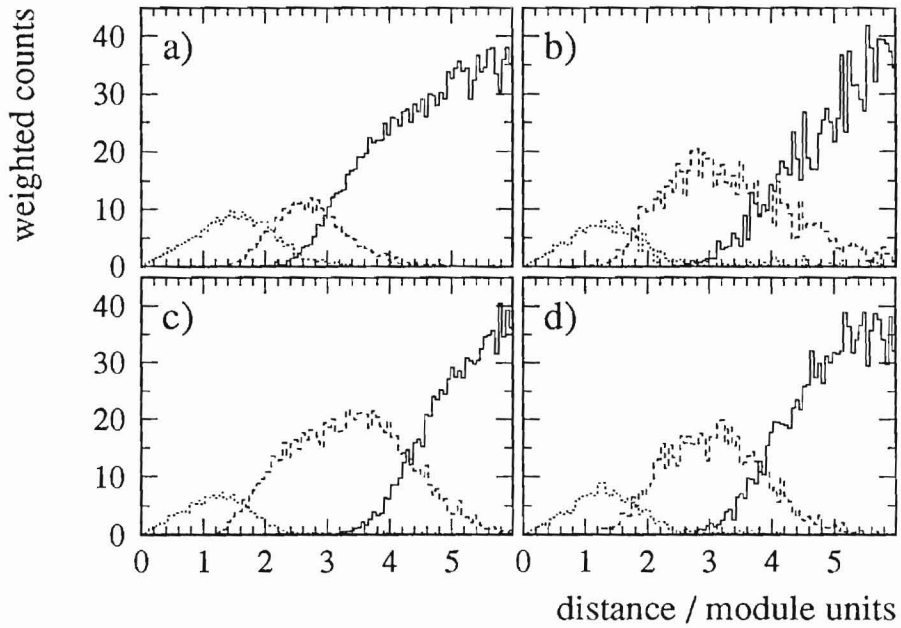

Figure 12: Resulting cluster type for two superimposed showers as a function of distance of the two incident particles. The dotted lines correspond to one cluster with one maximum, the dashed line to one cluster with two maxima, and the solid line to two clusters with one maximum each.

a) 10 GeV e^- + $\leq$ 1.4 GeV π^-,
b) 10 GeV e^- + 1.8-6.3 GeV π^-,
c) 10 GeV e^- + 10 GeV e^-,
d) 10 GeV e^- + 3 GeV e^-.

The sum of the distributions has been normalized to $2\pi r$ to reflect the phase space density for cluster pairs.

6 Recognition of overlapping showers

In the next two sections the overlap of two showers will be discussed. According to our cluster routine the problem of two overlapping showers was divided into two cases: the resulting cluster has only one maximum or there are two or more maxima. To study this this effect an artificial overlap was generated from the experimental data by adding the ADC-values of different single-hit events. Fig. 12 illustrates for different particle combinations and for different energies that clusters with one maximum occur only for small distances of the two particles ($\leq$ 2 module units, dotted line). Clusters with two maxima are observed at distances from 2 to 4 module units (dashed line) and two well separated clusters with one maximum each appear at distances larger than 4 module units. We will first discuss the case of one cluster with one maximum and shall turn to the two maxima case in section 7.

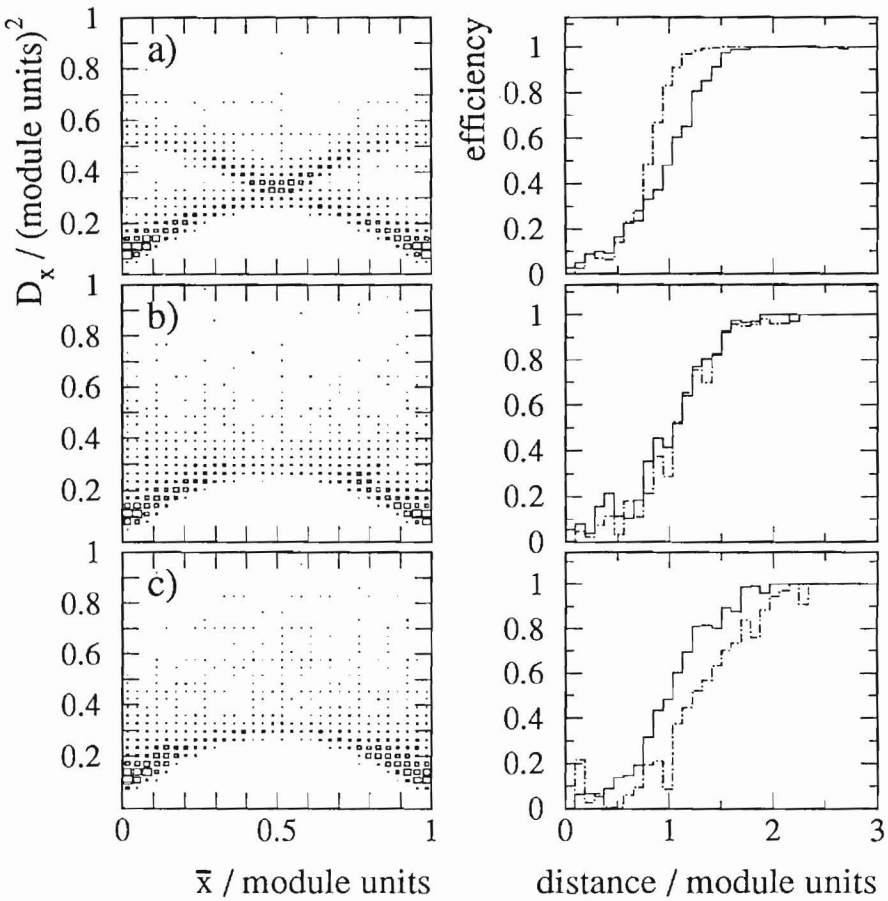

Figure 13: Dispersion D_x for two superimposed electromagnetic showers as a function of the corresponding first moment is shown (left column). The corresponding efficiencies to identify the overlap with a cut in D_{xy} (dashed line) and a cut in D_{xy}^{corr} (solid line) as a function of distance of the incident particles is displayed in the right column. From top to bottom the following combinations are shown :

a) 10 GeV e^- + 10 GeV e^-,
b) 10 GeV e^- + 3 GeV e^-,
c) 20 GeV e^- + 3 GeV e^-.

The overlap of two electromagnetic showers has been analyzed for three different energy combinations : a) 10 + 10 GeV, b) 3 + 10 GeV, and c) 3 + 20 GeV. Fig. 13 shows the second versus the first moment and the efficiency to reject these clusters as a function of the distance of the two incident particles for these combinations. The rejection has been performed by applying a cut on

$$D_{xy}^{corr} = \max(\, D_x^{corr},\, D_y^{corr}\,) \qquad \text{and} \qquad D_{xy} = \max(\, D_x,\, D_y\,). \tag{4}$$

The cut for these efficiencies corresponds to 10 % electron loss. As the lateral shape of electromagnetic showers is not very sensitive to the energy

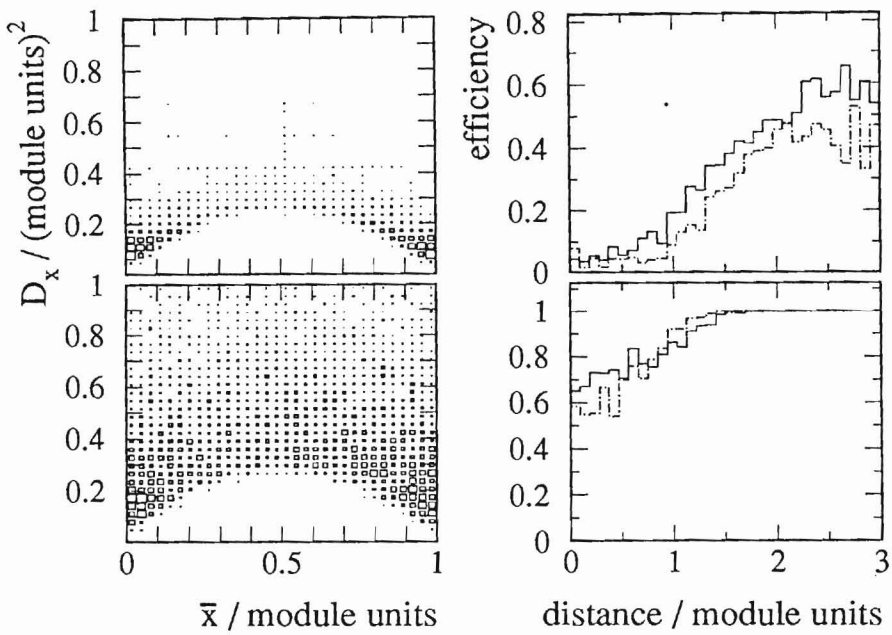

Figure 14: The same as Fig. 13, but here the following combinations are chosen :

upper figure: 10 GeV e^- + $\leq$ 0.9 GeV π^-,
lower figure: 10 GeV e^- + 5-15 GeV π^-.

it is expected that the recognition efficiency of such an overlap vanishes as the distance of the two showers becomes smaller. In the distance range from one to two module units, where these clusters are most likely (see Fig. 12), the efficiencies to identify an overlap are in all three cases around or above 50 %. For asymmetric energies a cut in D_{xy}^{corr} is more efficient than a cut in D_{xy}. Only in the special case that the two energies are similar a cut in D_{xy} is superior.

Fig. 14 shows the results for the superposition of a 10 GeV electron shower with a π^- depositing (a) less than 0.9 GeV and (b) between 5 and 15 GeV. The higher rejection efficiency of the cut in D_{xy}^{corr} compared to the cut in D_{xy} in Fig. 14 a) is in agreement with the results for two superimposed electromagnetic showers with different energies. The efficiency to reject an overlapping energetic hadronic shower is even for very small distances above 50 %, i.e. this kind of overlap will be recognized with a high efficiency.

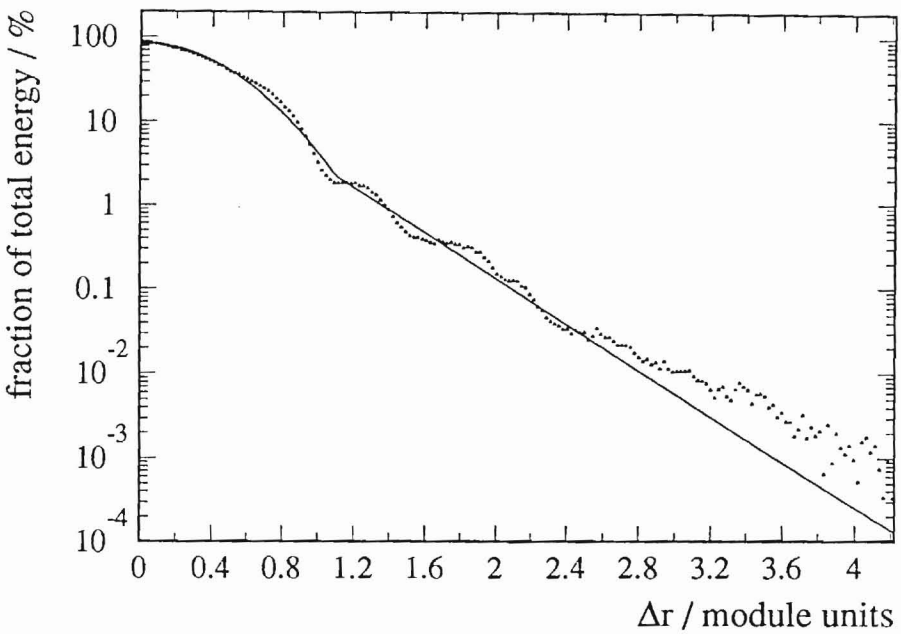

Figure 15: Response functions for 10 GeV electrons at (0°,0°). The radial response is calculated according to the detector coordinates neglecting the angle of incidence. Δr is the distance between the considered module and the first moment of the shower. The solid line represents a parameterization given in Eq. 5.

7 Unfolding of electromagnetic showers

In this chapter a method to unfold clusters with two maxima will be presented. The hypothesis is that each maximum indicates an electromagnetic shower. After unfolding each separated hit will be analyzed according to the dispersion D_{xy}^{corr}.

A necessary ingredient for this is the lateral response function of electromagnetic showers, which has been extracted from experimental data. The energy deposition is shown in Fig. 15 for 10 GeV electrons with perpendicular incidence. For simplicity, only the distance between the center of a module and the first moment of the shower is considered, which causes the oscillations in Fig. 15 and neglects the asymmetry in x and y for non-perpendicular angle of incidence. The following energy dependent function, which is superimposed in Fig. 15 to the data as a solid line, provides a rough parametrization for our data:

$$f(\Delta r, E) = A \ \max(\ \exp(-\Delta r^2/0.33),\ d\ \exp(-\Delta r/s)\ ) \tag{5}$$
$$s = 0.254 + 0.013\, E^{0.7}$$
$$d = 1.67 - 0.374\ \ln(E)$$

Here E is the energy of the electromagnetic shower in GeV, Δr the distance from the first moment in module units, and f a function, which has to be normalized to the measured ADC-channels by the parameter A. This parametrization is applicable as long as the module size is comparable to the Molière radius.

A flow chart of the unfolding algorithm is shown on the right hand side of Fig. 4. The unfolding procedure itself needs the estimated energies and positions of the single showers as input parameters. Start values for the energies and the positions are given by the two modules found as maxima by the cluster finding routine, i.e. the positions of the showers are given by the centers of these modules and their pulse heights are used for normalization of Eq. 5. The pulse height A_i of the i-th module of the cluster is subdivided into A_i^1 and A_i^2 according to the following formula :

$$A_i^k = \frac{f(\Delta r_{ik}, E_k)}{f(\Delta r_{i1}, E_1) + f(\Delta r_{i2}, E_2)} A_i \qquad \text{for } k = 1, 2 \qquad (6)$$

Here f_n is the normalized response function from Eq. 5. Only the relative normalization of the two showers is needed in this algorithm. For the unfolded hits new energies and positions are calculated, which are used as the input parameters for the next unfolding iteration. The next iteration is only performed, if at least one first moment has changed by more than 0.01 module units, otherwise the unfolding procedure is considered to have converged. The mean number of iterations has been found to be 2.5. As in the previous section, first the overlap of two electromagnetic showers and then the overlap of an electromagnetic with a hadronic shower will be discussed.

Electromagnetic showers of different energies have been unfolded and the reconstructed position and energy have been compared to the original single shower values. Fig. 16 shows results from the unfolding of clusters generated by 3 GeV and 10 GeV electrons. The energy- and spatial-resolution is similar to the single particle resolution for distances of the two particles of more than 2 module units, which is the most frequent case (see Fig. 12 d). For distances less than two module units the energy- and spatial-resolution worsens especially for the low energetic shower.

The ADC sum of overlapping clusters is larger than the sum of the single hits. ADC values, which are below the software threshold, contribute to the ADC sum for the case of artificial overlapped showers, if energy from the second hit is deposited in the same module.

The average change of the distance between the unfolded showers, measured by the first moments of the showers, depends on the distance of the two hits and is about -0.2 mm for the most frequent distances. Tab. 3 shows results for the unfolding of other energy combinations, which show a similar behavior to the ones discussed above.

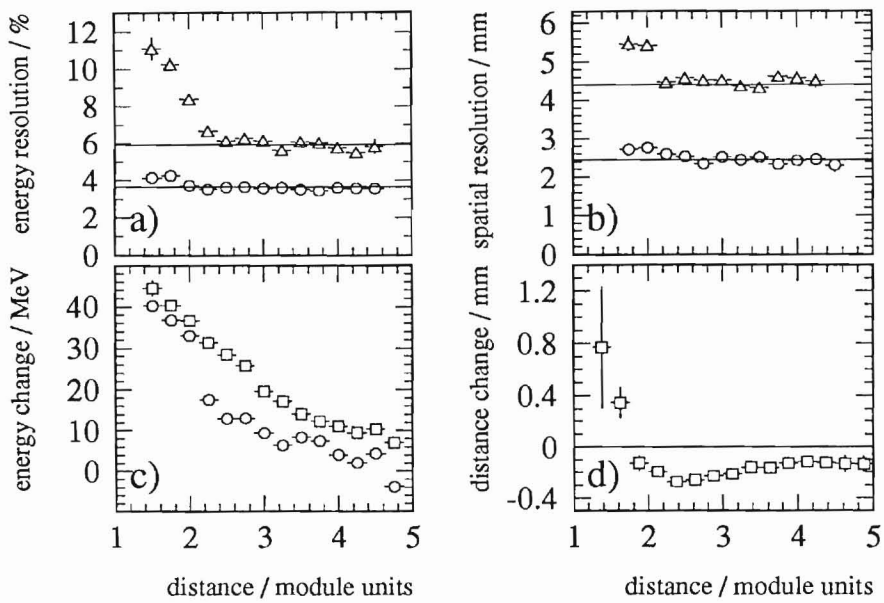

Figure 16: Results from the unfolding of an 3 GeV e^- (triangles) and an 10 GeV e^- (circles) as a function of the distance of the two showers. The solid lines in figure a) and b) represent the single e^- resolution.

a) energy resolution
b) spatial resolution
c) mean change of the e^- energy. The squares correspond to the energy gain of whole cluster. The reason for the energy increase is the ADC threshold. The circles show the energy gain of the 10 GeV e^-.
d) mean change of the distance between two first moments of the two showers.

Electrons have been overlapped with charged pions at an incident energy of 10 and 40 GeV, respectively. Due to the fluctuating energy release of the charged pions (see Fig. 2) two cases are analyzed, namely one with less than 0.9 GeV and one from 5 GeV to 15 GeV deposited energy. The energy- and spatial-resolution of the electrons is only slightly influenced by pions depositing little energy (see Tab. 4). If the charged pions deposit quite a large amount of energy, the energy- and spatial-resolution of the electrons becomes worse. Energy deposited by the pion is carried to the electron.

The effects of overlap of showers on the particle identification are illustrated in Fig. 17. All histograms show the fraction of particles, which yield a second moment D_{xy}^{corr} larger than the threshold used for particle identification. For electron-induced showers this corresponds to the number of electrons falling outside the electron identification window, whereas for pions it constitutes the fraction of showers, which were successfully rejected.

Three different compositions of overlapping showers are investigated: a) a 3 GeV electron and a 10 GeV electron, b) a pion, which deposits less than 0.9 GeV, and a 10 GeV electron, c) a pion, which deposits 5-15 GeV, and a 10 GeV electron. In the first two cases, where the 10 GeV

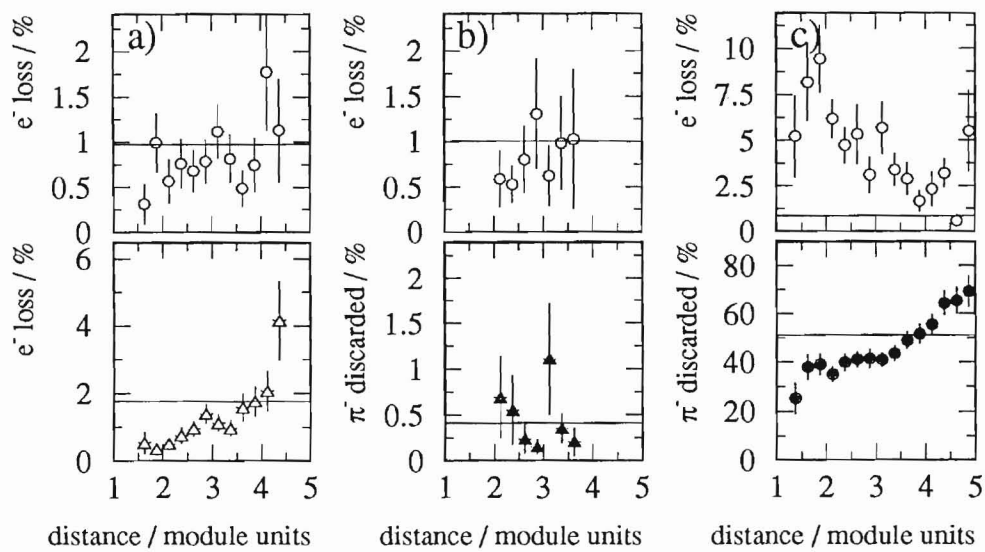

Figure 17: Particle identification for unfolded showers. The portion of particles with a second moment D_{xy}^{corr} larger than the cut used for the particle identification is plotted for three different combinations of overlapped particles. The solid lines represent the results obtained for single insulated hits.

a) 10 GeV e^- and 3 GeV e^-
b) 10 GeV e^- and $\leq$ 0.9 GeV π^-
c) 10 GeV e^- and 5-15 GeV π^-

electron shower contributes the dominant fraction of energy to the cluster, no significant changes of its second moment are observed. On the other hand, the dispersion of the unfolded 3 GeV companion (case a) appears to be reduced compared to isolated showers of the same energy, so even less of these electrons are lost by the dispersion analysis. The second moments of hadron-induced showers resulting in only small energy depositions (case b) also do not show any significant change by the unfolding. Please note, however, that only 0.4 % of those hits can be discarded by their second moment. The situation in case (c) is similar to that in (a); the second moments of strongly fluctuating hadronic showers tend to be reduced by the overlap with the 10 GeV electron shower. Here, however, this leads to a worsening of the pion rejection. In addition, the electron showers are influenced by the fluctuations of the hadron showers, leading to increased second moments and thereby causing also an enhanced loss of electrons.

For the first two of the above studied examples the method described in Sect. 4 can be applied with comparable efficiency. These will also be the most frequent situations in a real environment (see next section). Only for the last discussed case (c), the efficiency for particle identification becomes worse. The probability of finding a hadron depositing a large amount of energy in an em-calorimeter, however, is very low, so that example (c) from above is a rather rare situation.

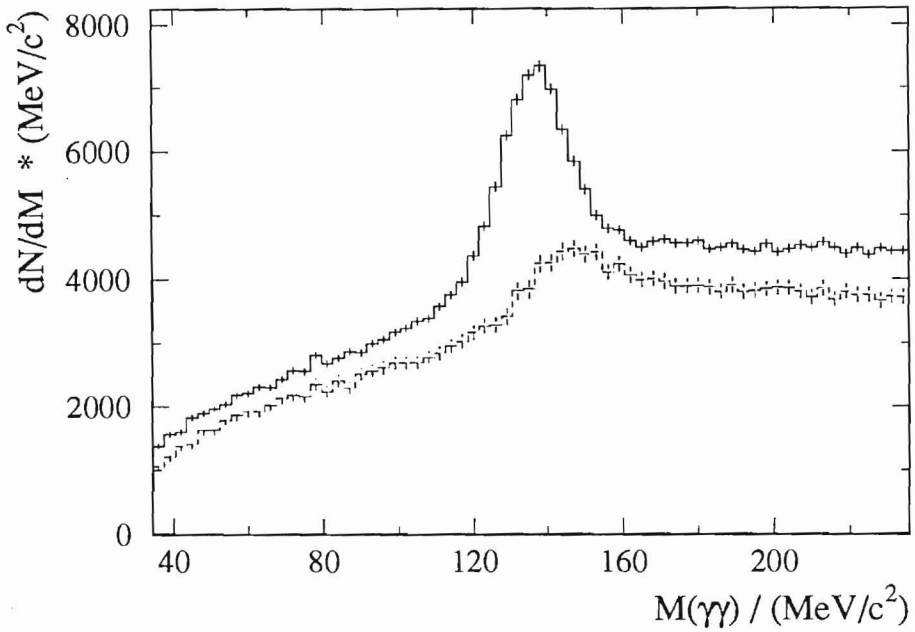

Figure 18: Two photon invariant mass spectra for 200 A·GeV ^{32}S+Au events. For the solid histogram only those hits have been used with a D_{xy}^{corr} value below 0.25, whereas the dashed histogram contains pairs where at least one D_{xy}^{corr} value is in the range from 0.25 to 0.5.

8 Application to heavy-ion data

The methods described in the previous sections can be applied to any laterally segmented em-calorimeter. In order to check the performance in a realistic experimental environment we have analysed data taken at the CERN SPS with the lead glass spectrometer SAPHIR in 200 A·GeV ^{32}S+Au reactions [12, 13]. The detector comprises 1278 lead-glass modules and is located at a distance of 9 m from the target, where it covers the pseudorapidity range from 2.3 to 2.9. The method was tested by analyzing the $\pi^0 \rightarrow 2\gamma$ decay observed in the two photon invariant mass spectrum. The π^0 mass resolution reflects the effective energy- and position-resolution of the detected hits [3, 11, 14]. In Fig. 18 invariant mass spectra are shown for the case that both D_{xy}^{corr} values are below 0.25 (solid histogram) and for the case that at least for one hit D_{xy}^{corr} is between 0.25 and 0.5 (dashed histogram). Fitting the mass spectra with a polynomial for the combinatorial background and a Gaussian for the π^0 peak reveals that the π^0 peak position μ increases from 135.1 $\pm$ 0.1 MeV/c^2 to 144.8 $\pm$ 0.4 MeV/c^2 as well as the width σ from 9.5 $\pm$ 0.2 MeV/c^2 to 11.8 $\pm$ 0.5 MeV/c^2. The sample of hits with larger second moments contains a considerable fraction of clusters, which originate from two showers, which cannot be unfolded. Such overlaps, e.g. from a photon and a minimum ionizing particle, will create

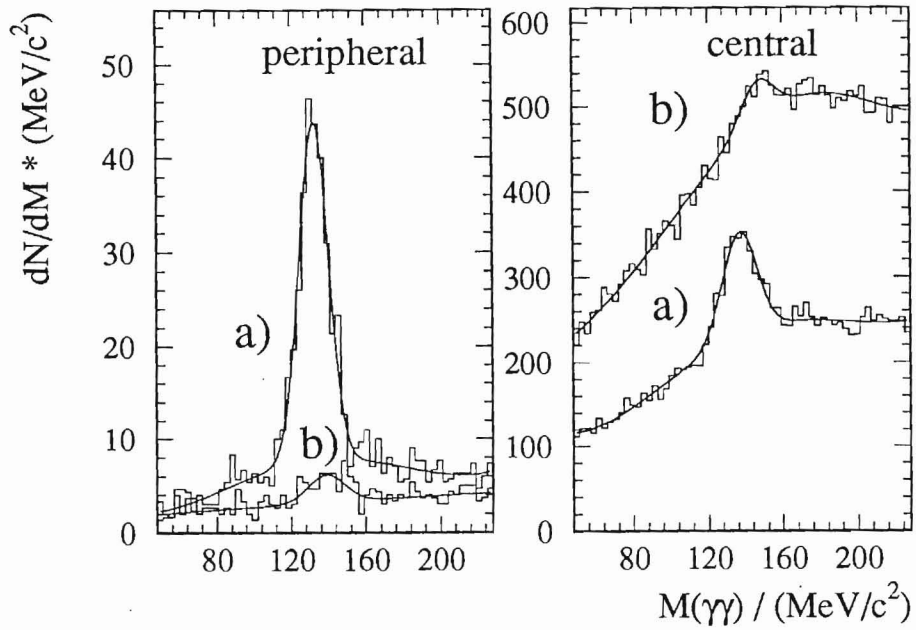

Figure 19: Two photon invariant mass spectra for 200 A·GeV ^{32}S+Au events. On the left hand side peripheral and on the right hand side central events are selected. a) only those hits having a D_{xy}^{corr} value below 0.25. b) at least one D_{xy}^{corr} value is above 0.25.

clusters, which have an energy slightly higher than the true photon energy. Such overlap effects will therefore result in a shift of the π^0 peak position and an increased width. The combinatorial background is comparable in both cases, although the π^0 peak content is 1/3 for the combinations with the higher D_{xy}^{corr} values. A detailed analysis of the π^0 peak as a function of D_{xy}^{corr} in the interval from 0. to 0.5 (module units)^2 shows that the π^0 peak position changes from 130 MeV/c^2 to 150 MeV/c^2 and at the same time the peak content normalized to the total number of entries in the mass window $\mu \pm 3\sigma$ decreases by a factor 3.5 from ≈ 0.32 to ≈ 0.09.

The effect of a high particle density has been analyzed by selecting central and peripheral, i.e. high and low multiplicity 200 A·GeV ^{32}S+Au events. Similar to Fig. 18 the following cut has been applied to the data displayed in Fig. 19 : a) both D_{xy}^{corr} values are below 0.25 and b) at least one D_{xy}^{corr} value is above 0.25. Due to the low particle density in peripheral events the influence of overlapping showers on the distribution of D_{xy}^{corr} is negligible — these reactions can therefore provide a test of the separation of hadrons and electrons. The distribution b) shows only a very small π^0 peak, i.e. nearly no photon is lost by the cut. In central reactions however, the higher overlap probability leads to a large number of hits, which cannot be used for π^0-reconstruction, but only contribute to the combinatorial

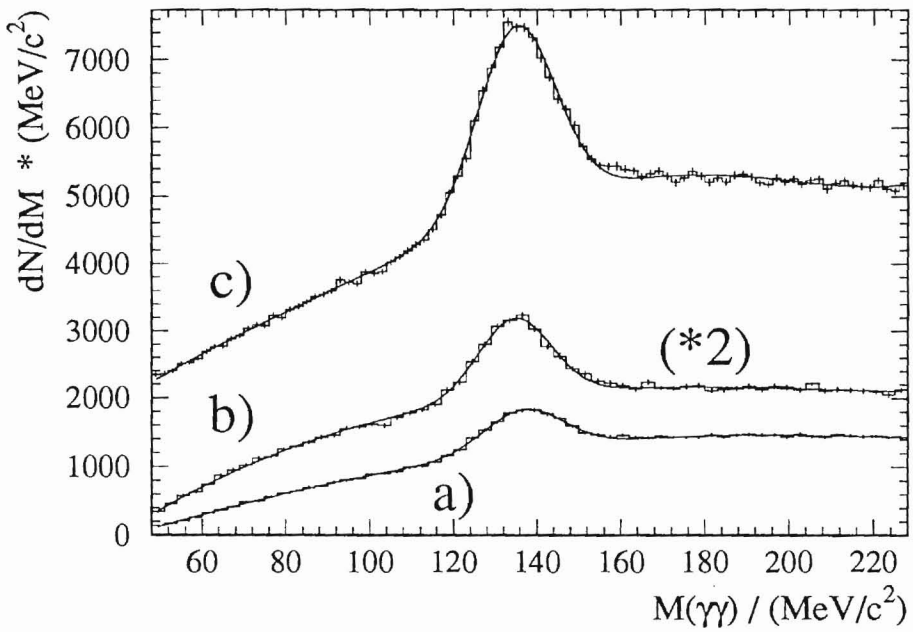

Figure 20: Two photon invariant mass spectra for 200 A·GeV ^{32}S+Au events in the interval 1 GeV/c $\leq |\vec{p_T}(\gamma\gamma)| \leq$ 2 GeV/c. Three different classes of hit combinations are chosen :

a) at least one photon has been unfolded from a cluster with 3 or more maxima,

b) at least one photon has been unfolded from a cluster with 2 maxima, and

c) all combinations are used regardless whether the hit has been unfolded or not.

background. The cut in D_{xy}^{corr} reduces the combinatorial background by a factor of 3 and at the same time the π^0 peak content is reduced by only 25%.

The unfolding of electromagnetic showers has been investigated in the same way by analyzing the two photon mass spectrum. In Fig. 20 invariant mass spectra are shown in the interval 1 GeV/c $\leq |\vec{p_T}(\gamma\gamma)| \leq$ 2 GeV/c for three different classes of hit combinations : a) at least one hit has been unfolded from a cluster with 3 or more maxima, b) at least one hit has been unfolded from a cluster with two maxima, and c) all combinations are used regardless whether the hit has been unfolded or not. The total π^0 peak content from a) and b) corresponds to $\approx$ 40 % of c). As the reconstruction efficiency of the π^0s is proportional to the square of the efficiency of the photons, the absolute photon reconstruction efficiency improves by about 30 % for the analyzed data sample.

A special problem occurs for the detection of hits originating from the same particle decay. According to the Lorentz boost the two decay photons

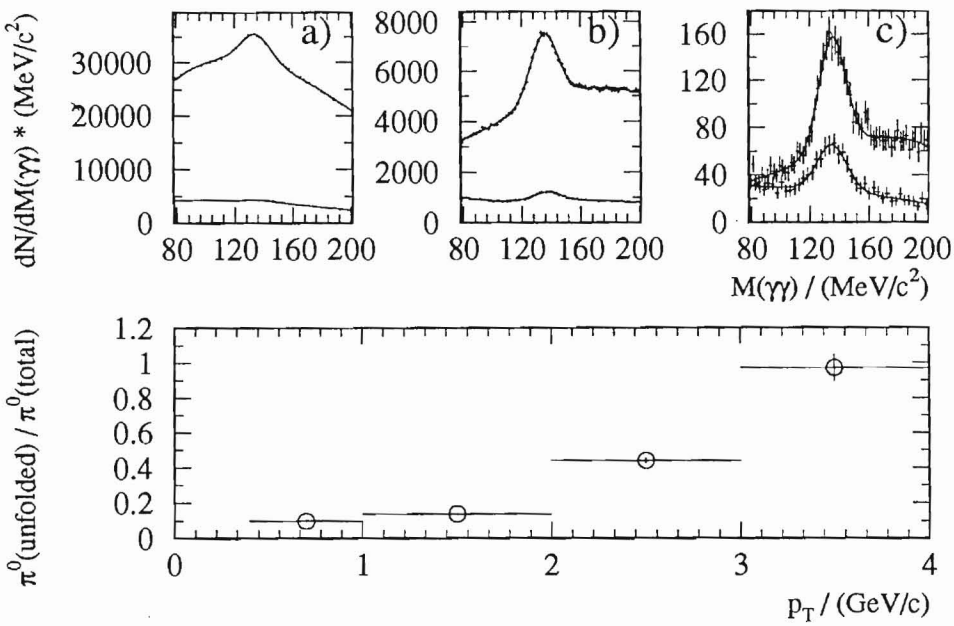

Figure 21: Two photon invariant mass spectra for 200 A·GeV ^{32}S+Au events in three intervals of $|\vec{p_T}(\gamma\gamma)|$:

a) 0.4 GeV/c $\leq |\vec{p_T}(\gamma\gamma)| \leq 1$ GeV/c
b) 1 GeV/c $\leq |\vec{p_T}(\gamma\gamma)| \leq 2$ GeV/c
c) 2 GeV/c $\leq |\vec{p_T}(\gamma\gamma)| \leq 3$ GeV/c

Two different classes of hit combinations are chosen : i) all combinations are used regardless whether the hits have been unfolded or not and ii) both hits have been unfolded from the *same* cluster.
For the ratio as a function of $|p_T(\pi^0)|$ see the text.

from a energetic π^0 tend to merge into one cluster. Therefore invariant mass spectra have been calculated in different bins of $|\vec{p_T}(\gamma\gamma)|$ for two classes of hit combinations : i) all combinations are used regardless whether the hit has been unfolded or not and ii) both hits have been unfolded from the *same* cluster. The resulting invariant mass spectra are displayed in Fig. 21. The amount of π^0s reconstructed by class ii) is also shown in Fig. 21 by plotting the ratio of these π^0s to all reconstructed π^0s as a function of $|\vec{p_T}(\pi^0)|$. Due to the high particle density of heavy-ion reactions this ratio is not vanishing even at low $|\vec{p_T}(\pi^0)|$ values, as the two photons may merge into one cluster by adding one or several showers in between them.

We would like to point out, that no significant effect on the π^0 peak position and width has been observed for the mass spectra including unfolded hits.

9 Summary

We have presented a simple and fast, but very effective method to identify electromagnetic and hadronic showers in modular em-calorimeters by analyzing the characteristic widths of the showers. The proposed method covers previously published algorithms [6,8] and is furthermore a generalization of them. Results obtained from data taken with a test box in electron and pion beams show that at 10 GeV deposited energy isolated hadronic showers can be rejected from em-showers with nearly 80% efficiency when accepting at the same time a 10% loss of electron induced showers. These figures are found to be independent of the angle of incidence with respect to the detector surface ($\Theta \leq 10°$). Furthermore, the identification (rejection) efficiency does not show any significant position dependence over the cross section of the detector modules, which constitutes an important improvement over former methods [6,8].

The identification and unfolding of overlapping showers has been investigated in great detail for various hit combinations. For two-hit clusters with one maximum detection efficiencies of more than 50% have been found for very small distances of 1–2 module units. If the second maximum appears, the original hit positions and energies are recovered with only little loss in position- and energy-resolution even for such small distances.

As a final and realistic test of the overall performance we have applied the proposed methods to data taken with a lead-glass detector in high energy heavy-ion reactions. The contents and width of the π^0 peak in the $\gamma\gamma$ invariant mass spectra was considered a quality scale for the reconstruction algorithm. Large improvements are observed particularly in central collisions with their associated high particle density; a clear π^0 peak occurs only after application of the cluster routines in the γ - γ pair combinations. The absence of the invariant mass peak in the γ - nonγ pair sample demonstrates the high photon reconstruction efficiency.

Acknowledgement

We are very much indebted to the members of the WA80 Collaboration at CERN for helping to perform the test experiment as part of a larger measurement. Special thanks go to our colleagues from the Kurchatov Institute at Moscow for contributing the TF1 lead-glass and the FEU-84 photomultipliers. We are grateful also to N. Heine for his substantial technical support and help during the run.

Literatur

[1] C. W. Fabjan et al., Nucl. Instr. Meth. **141** (1977) 61
C. W. Fabjan and H. G. Fischer, Rep. Prog. Phys. Vol. **43** (1980) 1003-1063
C. W. Fabjan and T. Ludlam, Ann. Rev. Nucl. Part. Sci. **32** (1982)
U. Amaldi, Phys. Scripta **23** (1981) 409

[2] R. Brun et al., CERN-report **DD/EE/84-1** September 1987, GEANT 3.14/2, revised version

[3] H. Baumeister et al., Nucl. Instr. Meth. **A 292** (1990) 81-96

[4] T. C. Awes, private communication
B. Roters, Diploma thesis, University of Münster (1991)

[5] G. A. Akopjanov et al., Nucl. Instr. Meth. **140** (1977) 441-445

[6] V. A. Davydov et al., Nucl. Instr. Meth. **145** (1977) 267-270

[7] J. J. Gomez et al., Nucl. Instr. Meth. **A 262** (1987) 284-290

[8] T. C. Awes, private communication
M. Hartig, Diploma thesis, University of Münster (1991)

[9] F. Bianchi et al., Nucl. Instr. Meth. **A 279** (1989) 473-478

[10] A. De Angelis, Nucl. Instr. Meth. **A 271** (1988) 455-463
E. Longo and I. Sestili, Nucl. Instr. Meth. **128** (1975) 283-307
M. Della Negra, Physica Scripta, Vol. **23** (1981) 469-479

[11] R. Albrecht et al., Z. Phys. C - Particles and Fields **51** (1991) 1-10

[12] G. Clewing, Doctoral Thesis, University of Münster (in preparation)

[13] G. Hölker, Doctoral Thesis, University of Münster (in preparation)

[14] L. Dragon, Doctoral Thesis, University of Münster (1989)

Tables

energy	θ_x	θ_y	*events*	θ_x	θ_y	*events*
3 GeV	2°	0°	11050	4°	4°	11260
10 GeV	0°	0°	19501	4°	4°	11156
	6°	0°	12836	2°	2°	10653
	6°	6°	10496	2°	0°	10993
	4°	0°	12181			
20 GeV	0°	0°	15086	4°	4°	10248
30 GeV	0°	0°	18881	4°	4°	9777

Table 1: Number of measured e^- events. $\theta_x(\theta_y)$ are the angles with respect to the perpendicular incidence.

energy	θ_x	θ_y	*events*
3 GeV	0°	0°	1060
5 GeV	0°	0°	4266
10 GeV	0°	0°	16580
20 GeV	0°	0°	26279
30 GeV	0°	0°	32700
40 GeV	0°	0°	38223

Table 2: Number of measured π^- events. $\theta_x(\theta_y)$ are the angles with respect to the perpendicular incidence.

	3 + 10 GeV e^-		3 + 30 GeV e^-		10 + 30 GeV e^-	
beam energy / GeV	3	10	3	30	10	30
single-hit energy res.	5.9 %	3.6 %	5.9 %	2.6 %	3.6 %	2.6 %
unfolded hits	6.6 %	3.8 %	6.2 %	2.4 %	4.2 %	2.9 %
energy change / MeV	11.5	12.0	9.5	17.8	23.0	16.5
single-hit spatial res. / mm	4.4	2.4	4.4	1.7	2.7	1.7
unfolded hits / mm	4.8	2.6	4.9	1.7	2.8	1.7
distance change / mm	−0.17		−0.10		−0.08	
$< \Delta D_x >$ / (module units)^2	0.0047	0.0016	0.0064	0.0002	0.0026	0.0013
$\sigma(\Delta D_x)$ / (module units)^2	0.031	0.017	0.033	0.015	0.025	0.017

Table 3: Energy resolution and spatial resolution of unfolded e^- compared to single particle resolutions and the change of D_x. ΔD_x is the change of D_x caused by the unfolding algorithm.

	40 GeV π^- + 10 GeV e^- $E_{\text{dep.}}(\pi^-) < 0.9$ GeV		40 GeV π^- + 10 GeV e^- 5 GeV $< E_{\text{dep.}}(\pi^-) <$ 15 GeV	
	π^-	e^-	π^-	e^-
single-hit energy res.		3.6 %		3.6 %
unfolded hits		3.6 %		4.7 %
energy change / MeV	26.9	−20.5	−205	236
single-hit spatial res. / mm		2.4		2.4
unfolded hits / mm		2.5		2.9
distance change / mm	−1.47		2.25	
$< \Delta D_x >$ / (module units)^2	−0.0029	0.0322	−0.0514	0.0393
$\sigma(\Delta D_x)$ / (module units)^2	0.013	0.050	0.084	0.054

Table 4: Energy resolution and spatial resolution of unfolded e^- from an overlap between an e^- and a π^- compared to single particle resolutions and the change of D_x. ΔD_x is the change of D_x caused by the unfolding algorithm.